Insights into the electronic structure and vibrational dynamics of Li 7 MnN 4 anode material for Li-ion battery: a combined experimental and computational study

Y. Zhou, E.M. Roginskii, K.S. Smirnov, M.B. Smirnov, A.V. Savin, O. Nguyen, J.-P. Pereira-Ramos, R. Baddour-Hadjean

Insights into the electronic structure and vibrational dynamics of Li_7MnN_4 anode material for Li-ion battery: a combined experimental and computational study

Y. Zhou[a,b], E.M. Roginskii[c,*], K.S. Smirnov[d], M.B. Smirnov[e], A.V. Savin[c], O. Nguyen[b], J.-P. Pereira-Ramos[a], R. Baddour-Hadjean[a,*]

[a] *Institut de Chimie et des Matriéaux Paris-Est (ICMPE), UMR 7182 CNRS et Université Paris-Est Créteil, 2 rue Henri Dunant, 94320, Thiais, France*
[b] *Tenchnocentre Renault, 1 Avenue du Golf, 78280, Guyancourt, France*
[c] *Ioffe Institute, Polytekhnicheskaya 26, 194021, St. Petersburg, Russia*
[d] *Univ. Lille, CNRS, UMR 8516 – LASIRe – Laboratoire Avancé de Spectroscopie pour les Interactions, la Réactivit et l'Environnement, 42 Rue Paul Duez, 59000, Lille, France*
[e] *St. Petersburg State University, 7/9 Universitetskaya nab., 199034, St. Petersburg, Russia*

Abstract

The electronic structure of the promising Li-ion battery ~~(LIB)~~ anode material Li_7MnN_4 ~~(LMN)~~ synthesized by a solid-state reaction is studied using *ab inito* calculations completed by Raman spectroscopy experiments. The structural optimization reliably reproduces the experimental one, hence validating the accuracy of the chosen Density Functional Theory method. The theoretical analysis of the electronic structure reveals the nature of the valence band as composed from band filled by electrons with spin-up states only, which allows refuting literature data about the claimed electronic character of ~~LMN~~Li_7MnN_4. Actually, the calculated electronic band gap $E_g = 0.95$ eV is found to be in good agreement with available experimental data. A careful experimental approach provides the first experimental Raman spectra of hydroscopic ~~LMN~~Li_7MnN_4 at 293 K and 130 K. The analysis of the phonon states in the Γ-point of the Brillouin zone, completed by the computation of the Raman scattering intensities of the vibrational modes of the ~~LMN~~Li_7MnN_4 structure give a remarkable agreement between simulated and experimental Raman spectra. With such a good matching, a reliable assignment of all the observed Raman peaks to the vibrations of specific structural units in the ~~LMN~~Li_7MnN_4 lattices is proposed. In particular, the most intense band in the Raman spectrum is ascribed to a totally symmetric MnN_4 breathing mode. We also show that, using different wavelengths of exciting radiation, the transition from off-resonance to resonance Raman scattering process can be observed. Furthermore, Raman spectroscopy is revealed as an efficient *in situ* diagnostic tool to control the degradation of

*Corresponding author
Email addresses: e.roginskii@mail.ioffe.ru (E.M. Roginskii), baddour@icmpe.cnrs.fr (R. Baddour-Hadjean)

the ~~LMN~~Li_7MnN_4 powder in open air through the observation of extra bands in the Raman spectra. Results of this study shed a light on the understanding of the fundamental properties of ~~LMN~~Li_7MnN_4 and pave a way for the upcoming operando Raman spectroscopy investigation of the atomic-scale induced structural changes of this negative electrode material for ~~LIB~~Li-ion battery.

Keywords: *ab initio*, Raman, Electronic structure, Lithiated transition metal nitrides, Li_7MnN_4, Anode material, Li-ion batteries

---

1. Introduction

Lion batteries (LIBs) are considered as one of the most important energy storage technologies for the modern society owing to their light weight and high energy density, which explains their ubiquity in electronic portable devices. With the urgent need for decreasing greenhouse gas emissions of road transportation, a surge of the demand for LIBs is foreseen for the electric vehicles (EV) application in the near future. As the part of intermittent sustainable energy in the grid is increasing quickly, LIB is also an important technology for large-scale energy storage. Tremendous and continuous research has been achieved in this field over the past decade [1, 2, 3, 4].

Commercial LIBs have multiple choices for cathode materials such as layered oxides ($LiCoO_2$, $LiNi_{1-y-z}Mn_yCo_zO_2$, $LiNiCoAlO_2$...), spinel oxides $LiNi_xMn_{2-x}O_4$ as well as olivine $LiFePO_4$.[5] Such positive electrode materials are generally coupled with graphite negative electrode. Graphite delivers a large capacity (372 mAh g^{-1}) at a potential of 0.1-0.2 V vs Li^+/Li but suffers from the formation of solid electrolyte interphase (SEI), leading to poor rate capability and moderate cycling performance [6, 7]. The low lithiation potential of graphite could also generate Li plating at high rate, which decreases the lifetime of LIBs and may cause serious safety issues [8]. Lithiated transition metal oxide $Li_4Ti_5O_{12}$ (LTO) on the other hand, able to circumvent the problems of graphite [9], has been proposed as commercial anode material for some specific applications. Thanks to a high working potential (1.5 V vs Li) and minimal structural change during lithiation, the LTO anode material grants inherent security, excellent rate capability and good cycling performance. However, this is at the expense of a lower energy density due to a higher working potential than graphite and a moderate specific capacity ($\sim$150 mAh g^{-1} at 1C rate). Hence, considerable research efforts are still made toward more competitive anode materials such as alloy-dealloying metal (SiGeSnSb), metal oxides, metal nitrides, sulfides, phosphides, etc... [10, 11, 12] Among them, lithium transition metal nitrides ~~(LTMN)~~ are one of the most promising anode materials[1] which have gained much attention due to their appropriate working potential, large specific capacity and peculiar redox chemistry [13, 14, 15, 16, 17, 18, 19, 20, 21, 22, 23, 24].

Two groups of structure can be found in the ternary lithium transition metal nitride family: layered Li_3N-type and 3D anti-fluorite structures. In the case

of layered lithium transition metal nitrides, $Li_{2.6}Co_{0.4}N$ is considered as the most promising negative electrode material because of its large capacity (400–760 mAh g^{-1}) available in the 0.0–1.4 V potential range [15, 16]. In the same layered lithium transition metal nitride family, some of us have demonstrated the existence of $Li_{3-2x}Ni_xN$ and $Li_{3-2x}Co_xN$ nitrides as genuine Li intercalation compounds working in the 0.02–1 V potential range [21, 22, 23]. Among the lithium transition metal nitrides crystallizing in the 3D anti-fluorite structure, Li_7MnN_4 (LMN) has received most attention [14, 24, 25, 26, 27, 28, 29]new ref 25. Indeed, thanks to a working potential of 1.2 V, problematic Li plating can be avoided while enabling a higher full cell voltage than LTO. Moreover, compared to benchmark LTO, LMN delivers a much larger specific capacity of 250 mAh g^{-1} at 1C rate [24]. Excellent cycling performance were ascribed to limited structural changes of LMN on cycling, described as reversible unit cell breathing of ∼7 % [28]. Besides exhibiting remarkable electrochemical properties, LMN shows unique redox chemistry : the nominal oxidation state of Mn in LMN is +5, which is unusual and very high for Mn, and can even more go up to 6+ and 7+ on electrochemical oxidation in $Li_{7-x}MnN_4$ [29]. Such peculiar redox properties deserve a full understanding of the electronic structure of LMN.

Among spectroscopic techniques, Raman spectroscopy seems to be the most suited to investigate the structure and electronic properties of electrode materials for LIBs [30]. In addition, with the support of calculations using Density Functional Theory (DFT), key structure-spectrum relationships can be provided for complex Li-host structures, as previously reported for vanadium-based oxides used as positive electrode materials in LIBs [31, 32, 33, 34]. However, Raman spectroscopy has little been applied for studying the vibrational dynamics of nitrides [35, 36, 37]. Furthermore, to the best of our knowledge, no Raman spectrum of LMN has been reported yet whereas a few experimental and theoretical papers of its electronic state lead to contradictory conclusions [38, 39, 40, 41]. Indeed, results of calculations interpret the electronic structure of LMN as a metallic [40, 41], but this conclusion contradicts with absorption experiments [41] (edge of absorption of 1050 nm corresponding to a band gap value $E_g = 1.18$ eV).

The present work reports the results of a combined experimental and computational study of the structure, electronic states and lattice dynamics of the LMN crystal, with a particular emphasis on the Raman active vibrational modes. This material was synthesized by solid state reaction and characterized by means of galvanostatic experiments, X-ray diffraction (XRD) and for the first time, by Raman spectroscopy. The comparison of the experimental and computational results evidences a remarkable agreement and allows us to propose a complete and reliable assignment of peaks in the Raman spectrum to vibrations of particular structural units.

The paper is organized as follows. The next section provides a summary of the experimental procedures used for the material synthesis and characterization, as well as the computational protocol. Then, the electrochemical and structural features of the LMN compound are presented, as well as the results of the structure optimization using DFT. This discussion is followed by the

analysis of the electronic structure using spin-unrestricted calculations. The last section focuses on the Raman spectroscopy study, providing experimental Raman spectra that are reliably assigned with the help of *ab initio* calculations.

2. Experimental and computational details

2.1. Material Synthesis

LMN was synthesized by a solid-state reaction from reagent grade Li_3N (Alfa-Aesar, -60 mesh 99.4%) and Mn metal (Alfa-Aesar, APS < 10 microns, 99.6%) as described in our previous work [24]. The Li_3N powder and Mn powder were thoroughly mixed in an agate mortar and then pressed into pellet (14 mm diameter and 6–8 mm thickness) under 10^3 kg cm^{-2}. A 15% molar excess of Li_3N was used to compensate its sublimation during the heat treatment. The pellet was then transferred into a rectangular alumina crucible that was placed in the middle of two other alumina crucibles filled with titanium sponge, then put into an airtight tubular stainless-steel reactor. The titanium sponge is inert to the reaction and serves to trap trace amount of oxygen and moisture during the reaction. The stainless-steel reactor was then heated in a tubular furnace at 750 C° during 12h under a continuous nitrogen gas flow (0.1 L/min). After the heat treatment, the sintered pellet was hand ground into fine powder during 15 minutes in an agate mortar. All manipulations were carried out in a glove box under dry argon atmosphere (p(O_2, H_2O) < 0.1 ppm).

2.2. Experiments

The XRD measurements were carried out with a Bruker D8 ADVANCE diffractometer equipped with a CuK_α radiation source and a LynxEye detector. To avoid any degradation of sample due to the contact with environment, the sample was placed in an airtight semi-sphere polymer holder during the data acquisition. The Rietveld refinements were performed on as-collected pattern using GSAS ExpGUI package [42, 43]. In the refinement, the atomic displacement parameters $U_{\rm iso}$ were constrained to be the same for all atoms of the same chemical element, *i.e.* all Mn had the same $U_{\rm iso}$ value and the refinement took into account a preferential orientation along the [222] direction found for the sample.

Galvanostatic experiments were performed in a two-electrode CR2032 coin-cell. The as-prepared LMN powder (70 % wt) was mixed with acetylene black (22 % wt) and PTFE (8 % wt) and then rolled into a thin sheet. Approximately 0.5 cm^2 sheet was pressed under 10^3 kg cm^{-2} onto a copper grid (12 mm in diameter) as working electrode. The mass loading was 5 mg cm^{-2}. A metalic lithium disk was used as auxiliary and reference electrode. The electrolyte used was 1 Mol L^{-1} $LiPF_6$ in ethylene carbonate (EC), diethy carbonate (DEC) and dimethyl carbonate (DMC) solution (1:1:1, v/v, Alfar Aesar). 3 round sheets (16 mm in diameter) of glass microfiber filter (Whatman $^{\rm TM}$, grade GF/A) were used as separators.

Raman spectra were measured in a back-scattering geometry using a LaBRAM HR 800 (Jobin-Yvon-Horiba) micro-Raman spectrometer (diffraction gratings: 600 lines/mm, spectral resolution: 1.5 cm^{-1}) equipped with a back illuminated charge coupled device detector (Spex CCD) cooled by the Peltier effect to 200 K. Different radiation sources were used, namely He−Ne laser ($\lambda_0 = 633$ nm) and tunable Ar^+ laser ($\lambda_0 = 514$ and 458 nm). Because of a high sensitivity of nitrides to moisture [44], the powdered LMN sample was placed in a specially designed airtight cell adapted for Raman experiments in the $100 - 300$ K temperature range. The spectra were recorded at temperature of 293 K and 130 K. For the low temperature experiments, the sample was cooled down by a flow of liquid N_2 vapor throughout the cell. The sample temperature was controlled with the accuracy of 1 K by using an Au/Fe thermocouple.

A LWD50 objective was used to focus the laser light to a spot size of 1 μm^2 on the sample surface. A D0.6 laser filter was used, which gives 25% of full laser power. No sample degradation was observed using these illumination conditions.

2.3. Computations

The spin-unrestricted calculations were carried out with CRYSTAL17 code[45, 46] using LCAO basis set of double-zeta quality [47]. The exchange-correlation energy was treated within the general gradient approximation (GGA) to DFT with the PBEsol exchange-correlation functional [48]. The integration of the Brillouin zone was performed over a $4 \times 4 \times 4$ grid of k-points chosen according to the Monkhors-Pack scheme [49]. The Kohn–Sham equations were solved iteratively with the convergence criterion 10^{-8} eV for the structure optimization and the criterion was tightened up to 10^{-10} eV for the calculation of the phonon states and optical properties. The equilibrium structure was obtained by minimizing the total energy with respect to both lattice parameters and atom positions with the convergence criterion $2.5 \cdot 10^{-3}$ eV A^{-1} for forces. Frequencies and displacements of atoms in the vibrational modes were computed by diagonalizing the Hessian matrix obtained by the numerical differentiation of the analytical energy gradient with respect to atomic coordinates. [50].

The Raman tensor $\boldsymbol{\alpha}^m$ of each vibrational mode m was calculated as the third order derivative of total energy with the coupled perturbed Kohn-Sham method[51]. The Raman spectrum $R(\omega)$ of a powder sample was simulated as [52]

$$R(\omega) = \sum_m \frac{(\omega_0 - \omega)^4}{\omega(1 - \exp(-\hbar\omega/k_B T))} \left(\zeta_m^2 + \frac{7}{45}\gamma_m^2\right)\delta(\omega - \omega_m), \qquad (1)$$

where the sum runs over vibrational modes, ω_0 and ω_m are the frequencies of the incident radiation and of the vibrational mode m, respectively. In (1), ζ_m and γ_m denote two rotational invariants of the Raman tensor, $\delta(x)$ is the Dirac delta function and the other symbols have their usual meaning. The rotational

invariants ζ_m and γ_m are given by [52]

$$\zeta_m = \frac{1}{3}\left(\alpha_{xx}^m + \alpha_{yy}^m + \alpha_{zz}^m\right), \tag{2}$$

$$\gamma_m^2 = \frac{1}{2}\left[(\alpha_{xx}^m - \alpha_{yy}^m)^2 + (\alpha_{yy}^m - \alpha_{zz}^m)^2 + (\alpha_{xx}^m - \alpha_{zz}^m)^2\right] + \frac{3}{4}\left[(\alpha_{xy}^m + \alpha_{yx}^m)^2 + (\alpha_{xz}^m + \alpha_{zx}^m)^2 + (\alpha_{yz}^m + \alpha_{zy}^m)^2\right] \tag{3}$$

with α_{ij}^m $(i,j = x,y,z)$ being the Cartesian components of the tensor $\boldsymbol{\alpha}^m$. For comparison with experimental spectra, the stick spectrum obtained with (1) was convoluted with a Lorentzian function with HWHM = 4 cm^{-1}.The stability of LMN was tested by calculating phonon dispersion curves over the entire Brillouin zone with supercell approach implemented in PHONOPY package[53] and the results are shown in Figure S1 in Supplementary Information (SI)

3. Results and Discussion

3.1. Electrochemistry

Figure 1 shows a typical galvanostatic cycling curve of LMN at C/5 rate (for LMN the current density at C rate I_c = 168 mA g^{-1}) in the potential window 0.9 V — 1.6 V *vs.* Li^+/Li. The wide voltage plateaus at 1.20 V for oxidation and 1.16 V for reduction correspond to the Mn redox process during the lithium de-intercalation and re-intercalation, respectively. As demonstrated in ref. 29, the redox process involves the electrochemical oxidation of Mn^{5+} in pristine LMN to Mn^{6+} and Mn^{7+} and the reduction of Mn^{7+} back to Mn^{6+} and Mn^{5+}. The presence of these high valence states of Mn is an unique example in ~~solid-state chemistry~~nitride chemistry of 3d metals. The electrochemical delithiation and lithiation reaction can be written as (4):

$$Li_7MnN_4 \rightleftharpoons Li_{7-x}MnN_4 + x\ e^- + x\ Li^+\ (0 \leq\ x\ \leq\ 1.8) \tag{4}$$

As shown in Figure 1, 1.8 lithium ions can be reversibly exchanged during oxidation/reduction of LMN, which corresponds to a specific capacity of 300 mAh g^{-1}. As reported by some of us, a small and highly reversible breathing of the LMN structure during the redox process [28] ensures an excellent cycle life with 96 % capacity retention at C rate after 100 cycles. [24]

3.2. Structural properties

LMN crystallizes in the $P\bar{4}3n$ space group[25], with a primitive cubic unit cell, as illustrated in Figure 2 and Figure S2 in SI. The Rietveld refinement of LMN XRD pattern, Figure S3, leads to a lattice parameter a = 9.561 Å, in good agreement with the experimental value of 9.555 Å reported by Cabana et al. [26]

The structure of LMN is built of MnN_4 tetrahedra and the inter-tetrahedral space is filled with Li atoms that stabilize the structure. In the primitive cubic

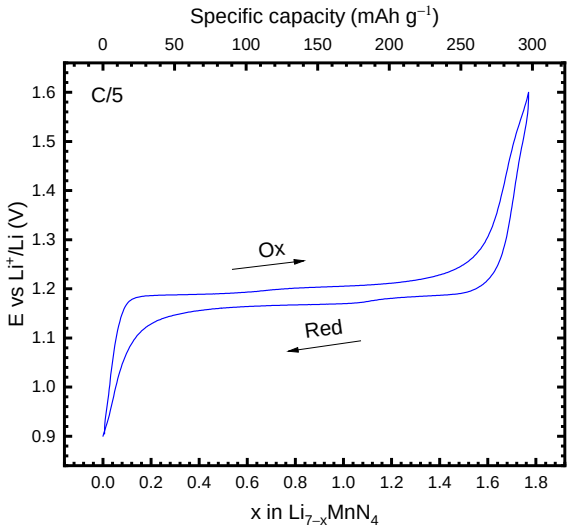

Figure 1: Galvanostatic cycling curve of LMN at C/5 rate (34 mA g^{-1}).

unit cell, the Mn atoms occupy 6*c* and 2*a* Wyckoff positions (WP) with local symmetry $\bar{4}$ and 23, respectively. The N atoms are situated in the general 24*i* and 8*e* WP with the local symmetry 3. The structure features two types of MnN_4 tetrahedra, Figure S2. Mn1 atoms situated on the surfaces of the cubic unit cell bonded to four N1 atoms, and Mn2 atoms situated on the vertices and in the center of the cubic unit cell bonded to four N2 atoms, form two types of tetrahedra hereafter referred to as "low-symmetry" and "high-symmetry" MnN_4 tetrahedra, respectively. Anticipating the forthcoming discussion, this structural peculiarity has a particular importance for the vibrational dynamics of the LMN structure. There are five symmetrically nonequivalent Li atoms in the unit cell. Two of them are located in high symmetry 6*b* and 6*d* WP with local symmetry 222 and $\bar{4}$. Two other Li atoms sit in low symmetry 8*e* and 12*f* WP, with local symmetry 3 and 2, respectively. The last Li atom occupies the general 24*i* WP.

Table 1 and table 2 list respectively the experimental and calculated atomic positions and bond lengths in LMN structure. It can be seen that a very good agreement is found between the two sets of structural experimental data and the results of the present DFT calculations. The calculated lattice parameter value of 9.514 Å differs by less than 0.5% from the experimental one. The comparison of the measured and simulated XRD patterns of LMN, shown in Figure 3, reveals also the good consistency between the calculated and experimental structural features. A good agreement between the calculated and experimental bond lengths values can be found as well with the only exception of Mn-N bonds that are by 4-6 % shorter in the calculations than in the experiment, Table 2. The results obtained from this whole structural analysis validate the accuracy of the

Table 1: Experimental and calculated atomic positions in the LMN unit cell ($P\bar{4}3n$) space group, No. 218.

Atom	WP	Experiment[a]	Experiment[b]	Experiment[c]	Calculation[d]
a, Å		9.57(1)	9.5548(3)	9.56077(11)	9.5142
		x=½	x=½	x=½	x=½
Mn1	6*c*	y=0.0	y=0.0	y=0.0	y=0.0
		z=¼	z=¼	z=¼	z=¼
Mn2	2*a*	x=y=z=0.0	x=y=z=0.0	x=y=z=0.0	x=y=z=0.0
		x=0.375	x=0.3582(2)	x=0.3629(6)	x=0.3563
N1	24*i*	y=0.375	y=0.3811(1)	y=0.3785(6)	y=0.3833
		z=0.125	z=0.1085(6)	z=0.1089(18)	z=0.1063
N2	8*e*	x=y=z=0.115	x=y=z=0.1095(6)	x=y=z=0.1155(17)	x=y=z=0.1089
		x=0.0	x=0.0	x=0.0	x=0.0
Li1	6*b*	y=½	y=½	y=½	y=½
		z=0.0	z=0.0	z=0.0	z=0.0
		x=¼	x=¼	x=¼	x=¼
Li2	6*d*	y=0.0	y=0.0	y=0.0	y=0.0
		z=½	z=½	z=½	z=½
Li3	8*e*	x=y=z=0.25	x=y=z=0.233(3)	x=y=z=0.2306(25)	x=y=z=0.231
		x=0.25	x=0.252(3)	x=0.2497(28)	x=0.25115
Li4	24*i*	y=0.25	y=0.236(3)	y=0.2446(27)	y=0.23862
		z=0.0	z=-0.014(3)	z=-0.021(4)	z=-0.01914
Li5	12*f*	x=0.25	x=0.257(5)	x=0.268(5)	x=0.263
		y=z=0	y=z=0	y=z=0	y=z=0

[a] Ref. 25
[b] Ref. 26
[c] This work. χ^2=2.718, Rwp=3.39 %, Rp=2.44 %, background: Chebyschev 12 parameters. (Figure S3, SI)
[d] This work.

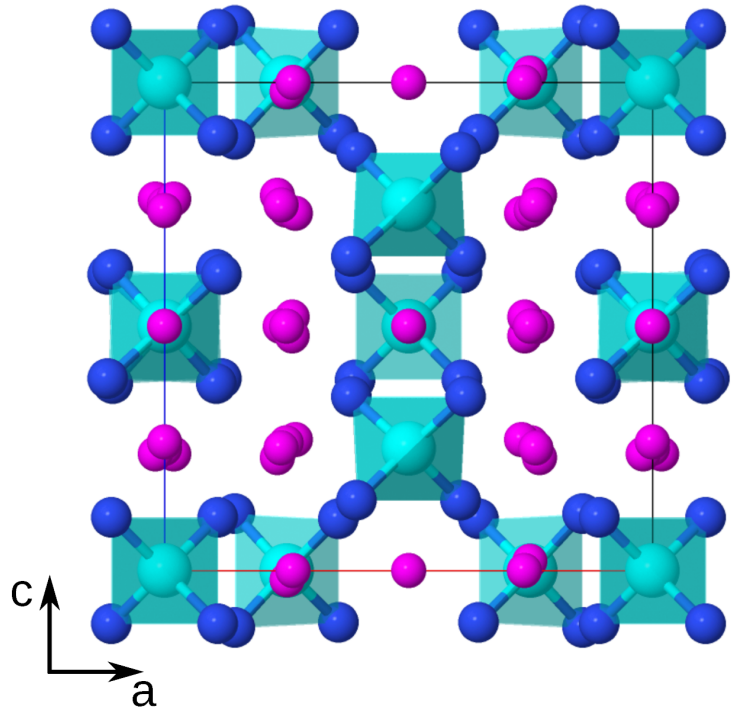

Figure 2: View of the LMN unit cell in the projection on the *ac* crystallographic plane. Color legend: cyan – manganese, blue – nitrogen, pink – lithium.

chosen DFT method to reproduce the experimental structure of LMN.

3.3. Electronic structure

To the best of our knowledge, only two studies have reported the electronic structure of LMN and both described this material as a metal with a partially occupied highest valence band. [40, 41] This picture is however doubtful in view of the optical absorption edge value of LMN, which was experimentally found at 1050 nm (1.18 eV) in ref. 41. Furthermore, as it will be shown below, LMN exhibits a characteristic Raman spectrum, which is quite unforeseen for a metal.

The calculated electronic band structure of LMN is plotted in Figure 4. One observes a significant difference between the spin-up and spin-down electronic states near the Fermi energy ($E = 0$) that emphasizes the need of using the spin-polarized calculations for the electronic structure analysis of this material. The valence band of the highest energy is built of 16 states with the spin-up polarization, while the conduction band of lowest energy has a mixed character and is composed of both spin-up and spin-down electronic states, Figure 4. The top of the valence band is found in the Γ-point and the bottom of the conduction band is in the R-point of the Brillouin zone. The calculated band gap value $E_g = 0.95$ eV is close to the experimental estimation of 1.18 eV

Table 2: Experimental and calculated lattice parameters (in Å) and bond lengths values of LMN. Bond length values between nitrogen atoms N2 and lithium ones are given in brackets.

	Exp.[a]	Calc.[a]	Calc.[b]
	Lattice Parameter		
a	9.561 Å	9.514 Å	9.555 Å
	Bond lengths		
Mn1–N1	1.911	1.811	1.818
Mn2–N2	1.913	1.799	1.803
Li1–N1(N2)	2.050 (2.038)	2.031 (2.031)	2.029
Li2–N1(N2)	2.088 (2.076)	2.121 (2.121)	2.126
Li3–N1(N2)	2.213 (2.225)	2.217 (2.140)	2.241
Li4–N1(N2)	2.102 (2.009)	2.079 (2.141)	2.155
Li5–N1(N2)	2.098 (2.110)	2.155 (2.155)	2.170

[a] This work.
[b] Ref. 40

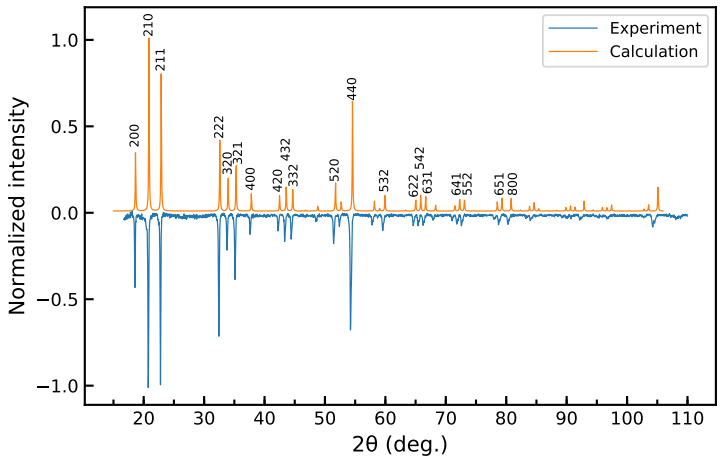

Figure 3: Experimental (after the background removal) and DFT simulated X-ray diffraction patterns of LMN. Peaks in the simulated XRD are labeled with *hkl* reflexion indices. The experimental pattern is negated for clarity.

from the absorption edge energy[41]. While PBEsol XC functional gives lattice constants of solids in a good agreement with experimental ones, the functional is known to underestimate band gap values.new ref 55[54, 55] The computed E_g can therefore be viewed as a lower theoretical estimate and LMN can be characterized as an indirect band gap semiconductor with a narrow gap.

The nature of the first valence band can be understood by the analysis of projected density of states (PDOS) shown in Figure 5. The peak in the total DOS just below the Fermi energy ($E = 0$ eV), Figure 5a, corresponds to the

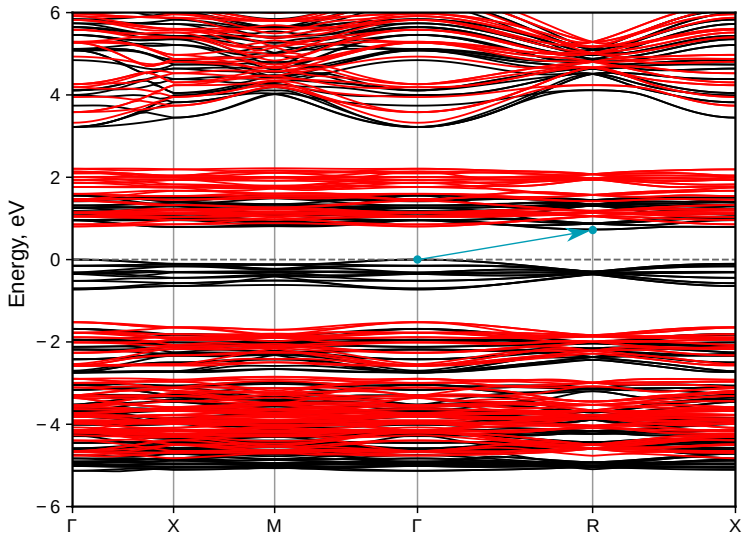

Figure 4: Calculated electronic band structure of LMN. Black and red curves stand for the branches of spin-up and spin-down electronic states, respectively. The origin of energy axis is placed at the Fermi energy indicated by the gray dashed line. The indirect optical transition is shown by arrow, see text for detail.

previously mentioned valence band with the spin-up states, Figure 4. Figure 5c and Figure 5d point to the major and nearly equal contributions of Mn and N atoms to the valence states, whereas the contribution of Li atoms to the band is almost negligible, Figure 5b. Furthermore, Figure 5e and Figure 5f show that the states are formed by the d-orbitals of Mn and p-orbitals of N atoms, respectively. It is worthy noting the absence of contribution from the valence $4s$ Mn orbitals to the band. This result suggests that two electrons occupying the orbital in free Mn atoms are engaged in bonding with N atoms in the LMN structure. The projected DOS for Mn in valence zone below -3.5 eV (Figure 5e) demonstrates some amount of electronic density for d-orbital which would be attributed to unpaired electron on 3d orbital of Mn atom. This statement reproduce the experimental results obtained from electron paramagnetic resonance spectra [38].

The Mulliken population analysis confirms this supposition. Indeed, the analysis for the Mn atoms shows an empty $4s$ orbital and five-fold occupied $3d$ orbitals, whereas the p-orbitals of nitrogens acquire an additional electron density. The Mulliken analysis yields the most stable configuration with the difference of number of the spin-up − spin-down states equal to 16.0 that agrees with the result obtained from the band structure examination.

3.4. Raman spectroscopy

The unit cell of LMN (multiplicity $Z = 8$) contains 96 atoms and therefore, the structure has 285 optical vibrational modes. The decomposition of the

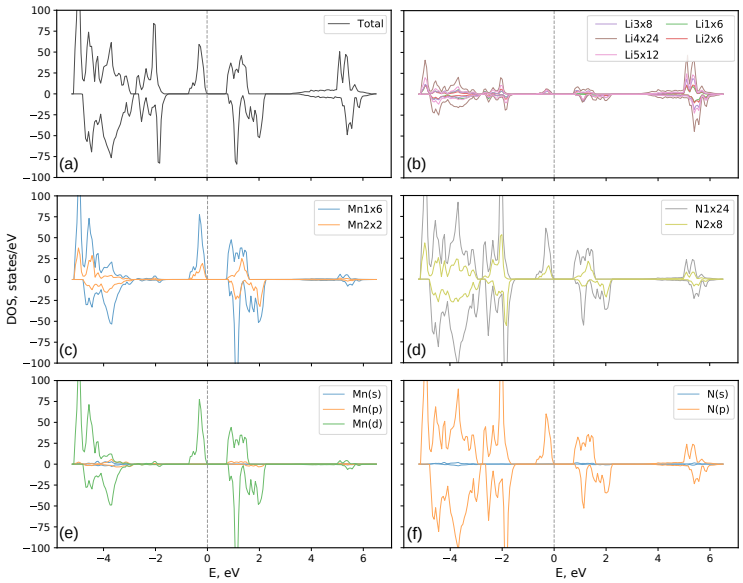

Figure 5: Calculated total (a) and projected (b) to (f) density of electronic states (PDOS) of LMN. PDOS in panels b) – d) are the density projected on the states of the Li, Mn and N atoms, respectively. Each PDOS in the panels b) – d) was scaled by a factor equal to the multiplicity of the corresponding Wyckoff position (Table 1). PDOS in panels e) and f) is the density projected on the valence orbitals of the Mn and N atoms, respectively. In all the panels, the density due to the spin-down states is negated for clarity.

modes in the irreducible representations of the $P\bar{4}3n$ space group in the Γ point of the Brillouin zone gives the following result:[56]

$$\Gamma_{optic} = 9A_1 + 11A_2 + 20E + 37T_1 + 38T_2. \quad (5)$$

Except the modes of A_2 and T_1 symmetry which are silent, all the other modes are Raman-active and one can therefore expect at most 67 peaks in the Raman spectrum of LMN. A complete analysis of the vibrational modes of LMN in the symmetry representations of the space group is given in Table S1 (SI).

The experimental Raman spectra of LMN recorded at 293K and 130K are plotted in Figure 6a, where they are compared with the Raman spectrum computed according to equation (1). Except a better resolution and a slight shift toward higher frequency for spectrum recorded at 130K, there is no significant different between these two Raman spectra. The discussion below will be mainly based on the spectrum recorded at 293K. Table 3 compares the positions of peaks in the experimental and calculated spectra. The simulated spectrum remarkably well reproduces the experimental spectra and a slight high-frequency shift of peaks in the computed spectrum compared with the experiment can be explained by a small underestimation of the calculated lattice parameter and the Mn-N bond, Table 2. For convenience of discussion, the spectrum in Figure 6a can be divided into three frequency regions, namely a low frequency

range (up to 450 cm^{-1}), Figure 6b; a medium frequency range (from 450 cm^{-1} to 600 cm^{-1}), Figure 6c and a high frequency range (600 cm^{-1} to 900 cm^{-1}), Figure 6d. The patterns of atomic displacements in the phonon modes with high intensities are displayed in Figures S4 (low frequency part of the Raman spectrum), S5 (medium frequency part) and S6 (high frequency part) in SI.

The low frequency region, Figure 6b, contains peaks related to modes resulting from the superposition of atomic displacements of Li and N atoms with the major contribution of the Li atoms. As the displacements of Li atoms produce small changes of the system polarizability, the corresponding peaks in the Raman spectra have low intensity. Positions of peaks in the calculated spectrum well correlate with those in the experimental spectra and the computed relative intensities are in a reasonable agreement with the experiment. The most intense peak 2 in this low frequency range, observed at 230 cm^{-1}, stems from a phonon with large-amplitude displacements of Li atoms, Figure S4b. The peak 6, observed at 362 cm^{-1}, corresponds to a phonon combining displacements of Li atoms with a deformation of $Mn1(N1)_4$ tetrahedra, Figure S4f whereas the peaks 7 and 8, observed respectively at 390 cm^{-1} and 410 cm^{-1}, correspond to Li displacements accompanied by deformation vibrations of the $Mn1(N1)_4$ tetrahedra, Figure S4g, S4h.

In the medium frequency region, Figure 6c, most peaks originate from the deformations and rotations of MnN_4 tetrahedra. Thus, the peak 9, observed at 438 cm^{-1}, can be related to the doubly degenerated vibrational mode of E symmetry that involves a distortion of the $Mn1(N1)_4$ tetrahedra, calculated at 457 cm^{-1}, Figure S5a. The most intense peak 10, observed at 454 cm^{-1}, can be assigned to two vibrational modes of the A_1 and E symmetry calculated at 461 cm^{-1} and 463 cm^{-1}, both yielding a distortion of the $Mn1(N1)_4$ tetrahedra that is accompanied by a displacement of lithium atoms sublattices, Figure S5b. The peaks 11 to 13, observed at 479, 503, 541 cm^{-1} respectively, are due to several modes that correspond to different deformations and rotations of the tetrahedra and to displacements of lithium atoms, Figure S5c,d,e.

The high frequency region of the spectrum contains the most intense peaks labeled 15 and 16, Figure 6d. Given its position and intensity, the peak 15 observed at about 700 cm^{-1} can be assigned to a totally symmetric A_1 mode at 701 cm^{-1} in the computed spectrum. The displacements of atoms in the mode are shown in Figure 7a and the mode can be characterized as a symmetric stretching vibration of the Mn-N bonds in the $Mn1(N1)_4$ tetrahedra (breathing mode). The in-phase change of the bond lengths results in a significant variation of the total polarizability that accounts for the high intensity of the corresponding peak in the spectrum. It is noteworthy that only the Mn–N bonds in "low-symmetry" $Mn1(N1)_4$ tetrahedra vary in the A_1 mode, whereas the Mn–N bonds of "high-symmetry" $Mn2(N2)_4$ tetrahedra remain unchanged.

According to our calculations, an analogous "breathing" mode, Figure S6c, of the $Mn2(N2)_4$ tetrahedra has a markedly higher frequency of 778 cm^{-1} and a very low Raman intensity. Such a difference between two counterpart modes of structurally similar MnN_4 tetrahedra requires a special discussion. In our opinion, this peculiarity is due to a different coordination of the N1 and N2

Table 3: Experimental and calculated frequencies (in cm^{-1}) of Raman active vibrational modes of the LMN structure.

	Experimental		Calculations		
Peak	T=293 K	T=130 K	A_1	E	T_2
1	172	178			194
2	230	232		229	
					270
3	291	292			289
4	306	309	297	300	
5	330	337			314
6	362	364			370
					379
7	390	391		384	384
				395	391
					397
8	410	412			409
					414
9	438	444		457	
10	454	459	463	461	
11	479	484	471	473	488
					492
12	503	509	514	510	513
					524
13	541	547		544	543
					551
			560		
14	662	671			668
15	696	702	701		
16	748	753	778	729	732

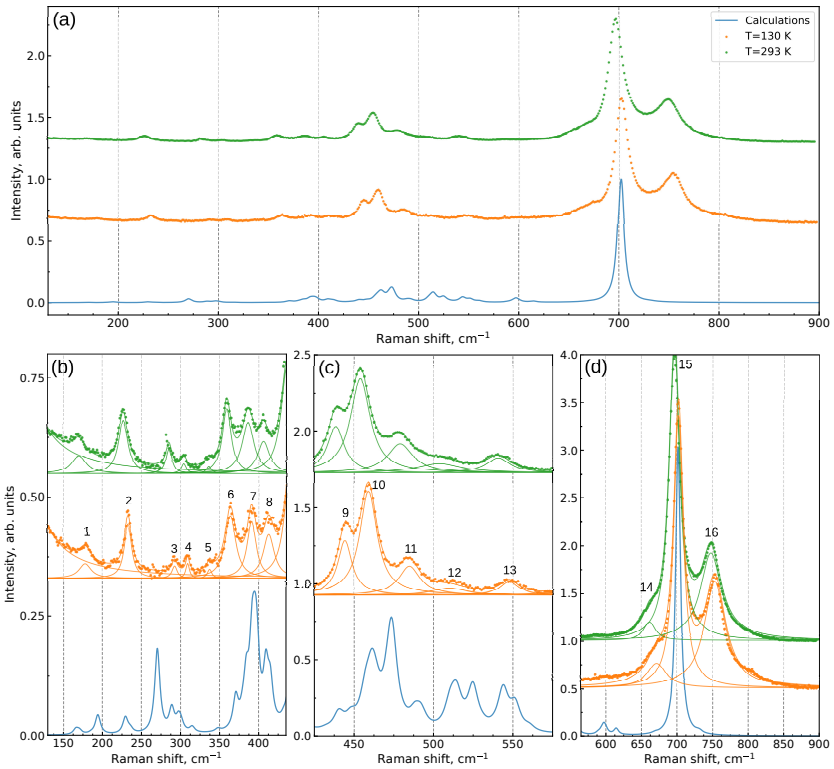

Figure 6: Experimental ($\lambda_0 = 633$ nm) Raman spectra of LMN recorded at T = 293 K (green color) and at T = 130 K (orange color), and the calculated (light blue color) spectrum of the compound. a) – general view; b) to d) – the spectra in different spectral regions as defined in the text. The panels b) – d) also display spectral components (thin lines) obtained by the deconvolution of the experimental spectra.

atoms by Li atoms. Given that the sum of ionic radii of the Li and N atoms is equal to 2.05 Å[57, 58], only the Li-N contacts shorter than 2.1 Å will be considered. Then, one finds that each N1 atom lies in the top of a trigonal NLi_3 pyramid with Li–N–Li angles of 114°–119°, Figure S7a, whereas an N2 atom is surrounded by four lithium atoms forming a tetrahedron, Figure S7b. It is also noteworthy that the N2-Li3 contact is the shortest one with the length of 2.02 Å and the Li3–N2–Mn2 atoms form a linear angle. In such structural subunits, the breating vibration of the $Mn1(N1)_4$ tetrahedron in the A_1 mode with the frequency of 701 cm^{-1} has a little impact on the length of the Li-N bonds in the $Li_6Mn1(N1)_4$ moiety, Figure S7a. On the other hand, the A_1 mode with the frequency of 778 cm^{-1} produces lengthening of the Mn2–N2 bonds and simultaneous shortening of the N2–Li3 bonds, Figure S7b. Therefore, such antiphase variations of the Mn2–N2 and Li3–N2 bonds account for the relatively high frequency and very low Raman intensity of this mode.

Because of its very low Raman intensity, the 778 cm^{-1} mode can hardly

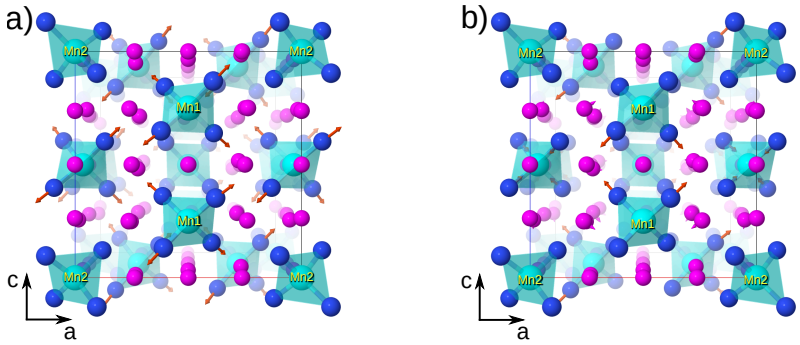

Figure 7: Atomic displacements in the modes at 701 cm^{-1} (a) and 729 cm^{-1} (b) corresponding to the peaks 15 and 16 in the Raman spectrum of LMN, respectively. Projection of the unit cell on the *ac* crystallographic plane is shown.

be related to the peak 16 observed at 750 cm^{-1}, Figure 6d. Instead, one can associate the peak 16 with the modes of E and T_2 symmetry computed at 729 cm^{-1} and 732 cm^{-1}, respectively. The former mode involves an asymmetric stretching vibrations of the $Mn1(N1)_4$ tetrahedra with two stretching and two shortening Mn-N bonds (atomic displacements are shown in Figure 7b). It is also noteworthy that the neighboring tetrahedra vibrate out-of-phase in the mode. The mode T_2 at 732 cm^{-1} has a similar nature but the atomic displacements are localized on the $Mn2(N2)_4$ tetrahedra, Figure S6b. The asymmetric character of the vibrational motion in the modes can account for a low Raman intensity of the corresponding peaks in the computed Raman spectrum, Figure 6d. Finally, low intensity peak 14 can be assigned to out-of-phase Li atom vibrational mode (Figure S6(a)) with symmetry T_2. As in the case of vibrational modes corresponding to the peak 16, the out-of-phase displacements of Li atoms in neighborhood planes leads to a very low Raman activity of the mode.

A difference in the intensity of some peaks in the computed and experimental spectra can also be attributed to the fact that the Raman spectra in Figure 6 were measured in electronic resonance conditions. Indeed, the energy of the exciting radiation ($\hbar\omega_0 \approx 1.96$ eV for $\lambda_0 = 633$ nm) is greater than the band gap estimated for LMN (0.95 eV). The dependence of the spectra on the wavelength λ_0 is displayed in Figure 8a. One can clearly see that the relative intensity of peaks 15 and 16 is strongly affected by the energy of the incident radiation.

As mentioned above, LMN is very sensitive to the moisture and has reactivity in air.[44] Figure 8b shows the Raman spectrum in the high-frequency range as a function of air exposure time. The spectrum recorded after 10 minutes air exposure still exhibits the intense peak 15 at 700 cm^{-1}, but a new broad band can be observed at 810 cm^{-1}. After 40 minutes air exposure, the relative intensity of this new component at 810 cm^{-1} has strongly increased, an additional peak has emerged at 770 cm^{-1} whereas the relatvie intensity of the peak 15 at 700 cm^{-1} has significantly decreased. In order to understand the nature of these new Raman features, an electrode made of the pristine LMN (with formula

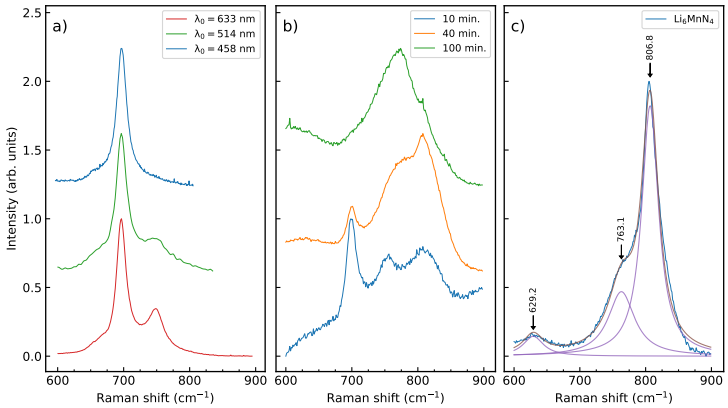

Figure 8: a) – Raman spectra of LMN powder sample in the airtight cell, measured with different wavelengths of the incident radiation λ_0. b) – Raman spectra of LMN powder sample obtained 10 min., 40 min., and 100 min. after opening the airtight cell, measured with λ_0=633 nm. c) – Raman spectrum of electrochemically oxidized Li_6MnN_4 electrode sample in the airtight cell, measured with λ_0=633 nm.

$Li_7Mn^{5+}N_4$ was electrochemically oxidized to $Li_6Mn^{6+}N_4$, then transferred in the airtight cell for Raman measurement. As shown in Figure 8c, the Raman spectrum of the electrochemically oxidized sample exhibits an intense band centered at 807 cm^{-1} which can be safely assigned to the vibration of N atoms with shorter distance to Mn^{6+} atoms. Since the new peak at 810 cm^{-1} for air-exposed samples (Figure 8b) coincides with the intense peak at 807 cm^{-1} in Li_6MnN_4, this suggests that the degradation process of LMN in air first involves the formation of the oxidized form of LMN, namely $Li_6Mn^{6+}N_4$ structural units.[44] For longer time of air exposure of LMN (100 min), Figure 8b, the decomposition process carries on: the 770 cm^{-1} band now dominates the Raman spectrum in the 600-900 cm^{-1} wave number range while the relative intensities of the characteristic Raman peaks at 700 cm^{-1} for Li_7MnN_4 and 810 cm^{-1} for $Li_6Mn^{6+}N_4$ units, have practically disappeared. This evolution strongly suggests the complete degradation of LMN after 100 min air exposure.

These results show that Raman spectroscopy is an efficient probe to control the integrity of the highly hygroscopic LMN sample and to monitor the oxidation state of Mn in the LMN anode material, as recently reported in the case of Ni in the $LiNi_{0.5}Mn_{1.5}O_4$ cathode.[59] This opens the opportunity for the study of the redox mechanism involved in LMN under electrochemical operation.

4. Conclusions

This paper presents the results of combined experimental and computational study of LMN structure and vibrational dynamics. This compound exhibits promising electrochemical performance for LiBs. In addition to high specific

capacity of 300 mAh g^{-1}, its operation voltage of 1.2 V allows a great improvement of battery safety. The structure of the compound was obtained using the Rietveld refinement of powder XRD data. The *initio* computed structural characteristics are in an excellent agreement with the experimental data. The electronic structure of the material was obtained in the spin-unrestricted calculations whose results enable us to characterize LMN as an indirect band gap semiconductor with a narrow gap and solve controversial literature data. The computed band gap of 0.95 eV is in a reasonable agreement with the experimental estimation obtained from the optical absorption edge energy ($\approx$ 1.18 eV) [41]. The calculations show that the electronic states at the top of the valence band are formed by the d and p states of Mn and N atoms, respectively, with spin up polarization only and the total spin amounts to 16 μ_B. The experimental Raman spectra of the compound were measured for the first time and their analysis was performed on the basis of the *ab initio* calculations. The analysis has allowed a reliable assignment of all prominent peaks in the spectra. The nature of most intense peak in Raman spectra is clarified by considering the symmetry of the crystalline lattice and that of the vibrational mode, it has been ascribed to a totally symmetric MnN_4 breathing mode at 700 cm^{-1}. We showed that Raman spectroscopy is a very efficient tool to monitor the manganese oxidation state in LMN and its reactivity in air. This combined experimental and computational Raman approach provides key structure-spectrum relationships, which is crucial for the further understanding of the atomic scale changes induced in LMN upon electrochemical operations.

5. Acknowledgement

A fellowship for E. M. R. from Université Paris-Est Créteil is gratefully acknowledged. A part of the calculations was performed using facilities of the Computational Center of Research Park of St.Petersburg State University. Part of the work is supported by the Renault Technocentre under the CIFRE contract No.2018/1610.

6. Author Information

6.1. ORCID

Yanlong Zhou: 0000-0002-1132-0443
Evgenii M. Roginskii: 0000-0002-5627-5877
Konstantin S. Smirnov: 0000-0002-8370-8797
Mikhail B. Smirnov: 0000-0002-4292-1989
Aleksandr V. Savin: 0000-0001-6778-6210
Olivier Nguyen:
Jean-Pierre Pereira-Ramos: 0000-0001-5381-900X
Rita Baddour-Hadjean: 0000-0002-3158-1851

6.2. Notes

Authors declare no competing financial interest.

References

[1] J.-M. Tarascon, M. Armand, Issues and challenges facing rechargeable lithium batteries, Co-Published with Macmillan Publishers Ltd, UK, 2010, pp. 171–179. doi:10.1142/9789814317665_0024.

[2] J. B. Goodenough, Y. Kim, Challenges for rechargeable Li batteries, Chemistry of Materials 22 (3) (2010) 587–603. doi:10.1021/cm901452z.

[3] J. B. Goodenough, K.-S. Park, The Li-Ion rechargeable battery: A perspective, Journal of the American Chemical Society 135 (4) (2013) 1167–1176. doi:10.1021/ja3091438.

[4] J. Liu, J.-G. Zhang, Z. Yang, J. P. Lemmon, C. Imhoff, G. L. Graff, L. Li, J. Hu, C. Wang, J. Xiao, G. Xia, V. V. Viswanathan, S. Baskaran, V. Sprenkle, X. Li, Y. Shao, B. Schwenzer, Materials science and materials chemistry for large scale electrochemical energy storage: From transportation to electrical grid, Advanced Functional Materials 23 (8) (2013) 929–946. doi:10.1002/adfm.201200690.

[5] M. S. Whittingham, Lithium batteries and cathode materials, Chemical Reviews 104 (10) (2004) 4271–4301. doi:10.1021/cr020731c.

[6] D. Aurbach, Review of selected electrode-solution interactions which determine the performance of Li and Li ion batteries, Journal of Power Sources 89 (2) (2000) 206–218. doi:10.1016/S0378-7753(00)00431-6.

[7] A. J. Smith, J. C. Burns, X. Zhao, D. Xiong, J. R. Dahn, A high precision coulometry study of the sei growth in Li/graphite cells, Journal of The Electrochemical Society 158 (5) (2011) A447. doi:10.1149/1.3557892.

[8] T. Waldmann, B.-I. Hogg, M. Wohlfahrt-Mehrens, Li plating as unwanted side reaction in commercial Li-Ion cells- A review, Journal of Power Sources 384 (2018) 107–124. doi:10.1016/j.jpowsour.2018.02.063.

[9] T. Ohzuku, A. Ueda, N. Yamamoto, Zero-strain insertion material of $Li[Li_{1/3}Ti_{5/3}]O_4$ for rechargeable lithium cells, Journal of The Electrochemical Society 142 (5) (1995) 1431–1435. doi:10.1149/1.2048592.

[10] S. Goriparti, E. Miele, F. De Angelis, E. Di Fabrizio, R. Proietti Zaccaria, C. Capiglia, Review on recent progress of nanostructured anode materials for Li-ion batteries, Journal of Power Sources 257 (2014) 421–443. doi:10.1016/j.jpowsour.2013.11.103.

[11] N. Tapia-Ruiz, M. Segalés, D. H. Gregory, The chemistry of ternary and higher lithium nitrides, Coordination Chemistry Reviews 257 (13-14) (2013) 1978–2014. doi:10.1016/j.ccr.2012.11.008.

[12] M. V. Reddy, G. V. Subba Rao, B. V. R. Chowdari, Metal oxides and oxysalts as anode materials for Li ion batteries, Chemical Reviews 113 (7) (2013) 5364–5457. doi:10.1021/cr3001884.

[13] M. Nishijima, Y. Takeda, N. Imanishi, O. Yamamoto, M. Takano, Li deintercalation and structural change in the lithium transition metal nitride Li_3FeN_2, Journal of Solid State Chemistry 113 (1) (1994) 205–210. doi:10.1006/jssc.1994.1360.

[14] M. Nishijima, N. Tadokoro, Y. Takeda, N. Imanishi, O. Yamamoto, Li deintercalation-intercalation reaction and structural change in lithium transition metal nitride, Li_7MnN_4, Journal of The Electrochemical Society 141 (11) (1994) 2966–2971. doi:10.1149/1.2059266.

[15] T. Shodai, Study of $Li_{3-x}M_xN$ (M: Co, Ni or Cu) system for use as anode material in lithium rechargeable cells, Solid State Ionics 86–88 (1996) 785–789. doi:10.1016/0167-2738(96)00174-9.

[16] T. Shodai, Reaction mechanisms of $Li_{2.6}Co_0.4n$ anode material, Solid State Ionics 122 (1-4) (1999) 85–93. doi:10.1016/S0167-2738(99)00038-7.

[17] R. Niewa, F. DiSalvo, D.-K. Yang, D. Zax, H. Luo, W. Yelon, Synthesis, crystal structure and properties of a lithium manganese nitride, $(Li, Mn)_2N$, Journal of Alloys and Compounds 266 (1-2) (1998) 32–38. doi:10.1016/S0925-8388(97)00456-8.

[18] R. Niewa, F. R. Wagner, W. Schnelle, O. Hochrein, R. Kniep, $Li_{24}[MnN_3]_3N_2$ and $Li_5[(Li_{1-x}Mn_x)N]_3$, two intermediates in the decomposition path of $Li_7[MnN_4]$ to $Li_2[(Li_{1-x}Mn_x)N]$: An experimental and theoretical study, Inorganic Chemistry 40 (20) (2001) 5215–5222. doi:10.1021/ic010412o.

[19] R. Niewa, Z.-L. Huang, W. Schnelle, Z. Hu, R. Kniep, Preparation, crystallographic, spectroscopic and magnetic characterization of low-valency nitridometalates $Li_2[(Li_{1-x}M_x)N]$ with M = Cu, Ni, Zeitschrift für anorganische und allgemeine Chemie 629 (10) (2003) 1778–1786. doi:10.1002/zaac.200300120.

[20] T. Y. Kim, M. G. Kim, J. M. Lee, T. Kang, H.-J. Sohn, Local structural variations of $Li_{2.6}Co_{0.4}N$ during the first charge and discharge, Electrochemical and Solid-State Letters 5 (5) (2002) A103. doi:10.1149/1.1465376.

[21] J. Ducros, S. Bach, J. Pereira-Ramos, P. Willmann, A novel lithium intercalation compound based on the layered structure of lithium nitridonickelates $Li_{3-2x}Ni_xN$, Electrochimica Acta 52 (24) (2007) 7035–7041. doi:10.1016/j.electacta.2007.05.037.

[22] J. B. Ducros, S. Bach, J. P. Pereira-Ramos, P. Willmann, Layered lithium cobalt nitrides: A new class of lithium intercalation compounds, Journal of Power Sources 175 (1) (2008) 517–525. doi:10.1016/j.jpowsour.2007.09.052.

[23] J. Ducros, S. Bach, J. Pereira-Ramos, P. Willmann, Comparison of the electrochemical properties of metallic layered nitrides containing cobalt, nickel and copper in the 1V—0.02V potential range, Electrochemistry Communications 9 (10) (2007) 2496–2500. doi:10.1016/j.elecom.2007.07.022.

[24] E. Panabière, N. Emery, S. Bach, J.-P. Pereira-Ramos, P. Willmann, Ball-milled Li_7MnN_4: An attractive negative electrode material for lithium-ion batteries, Electrochimica Acta 97 (2013) 393–397. doi:10.1016/j.electacta.2013.03.012.

[25] R. Juza, E. Anschütz, H. Puff, Die struktur von Li_7VN_4 und Li_7MnN_4, Angewandte Chemie 71 (4) (1959) 161–161. doi:10.1002/ange.19590710406.

[26] J. Cabana, N. Dupré, G. Rousse, C. P. Grey, M. R. Palacín, Ex situ NMR and neutron diffraction study of structure and lithium motion in Li7MnN4, Solid State Ionics 176 (29-30) (2005) 2205–2218. doi:10.1016/j.ssi.2005.07.001.

[27] E. Panabière, N. Emery, S. Bach, J.-P. Pereira-Ramos, P. Willmann, A kinetic study of electrochemical lithium insertion in Li_7MnN_4 by impedance spectroscopy, Journal of Alloys and Compounds 663 (2016) 624–630. doi:10.1016/j.jallcom.2015.12.121.

[28] N. Emery, E. Panabière, O. Crosnier, S. Bach, T. Brousse, P. Willmann, J.-P. Pereira-Ramos, In operando X-ray diffraction study of Li_7MnN_4 upon electrochemical Li extraction–insertion: A reversible three-phase mechanism, Journal of Power Sources 247 (2014) 402–405. doi:10.1016/j.jpowsour.2013.08.008.

[29] D. Muller-Bouvet, N. Emery, N. Tassali, E. Panabière, S. Bach, O. Crosnier, T. Brousse, C. Cénac-Morthe, A. Michalowicz, J. P. Pereira-Ramos, Unravelling redox processes of Li_7MnN_4 upon electrochemical Li extraction-insertion using operando XAS, Physical Chemistry Chemical Physics 19 (40) (2017) 27204–27211. doi:10.1039/C7CP05207C.

[30] R. Baddour-Hadjean, J. P. Pereira-Ramos, Raman microspectrometry applied to the study of electrode materials for lithium batteries, Chemical Reviews 110 (2010) 1278–1319. doi:10.1063/1.3482342.

[31] R. Baddour-Hadjean, M. B. Smirnov, K. S. Smirnov, V. Y. Kazimirov, J. M. Gallardo-Amores, U. Amador, M. E. A. de Dompablo, J. P. Pereira-Ramos, Lattice dynamics of β-v_2o_5 : Raman spectroscopic insight into the atomistic structure of a high-pressure vanadium pentoxide polymorph,

Inorganic Chemistry 51 (5) (2012) 3194–3201. doi:10.1021/ic202651b.
URL http://dx.doi.org/10.1021/ic202651b

[32] R. Baddour-Hadjean, M. Smirnov, V. Y. Kazimirov, K. Smirnov, J.-P. Pereira-Ramos, The Raman spectrum of the $\gamma\prime$-V_2O_5 polymorph: A combined experimental and DFT study, J. Raman Spectrosc. 46 (4) (2015) 406–412. doi:10.1002/jrs.4660.
URL http://dx.doi.org/10.1002/jrs.4660

[33] M. B. Smirnov, E. M. Roginskii, K. S. Smirnov, R. Baddour-Hadjean, J.-P. Pereira-Ramos, Unraveling the structure – raman spectra relationships in v_2o_5 polymorphs via a comprehensive experimental and DFT study, Inorganic Chemistry 57 (15) (2018) 9190–9204. doi:10.1021/acs.inorgchem.8b01212.

[34] E. M. Roginskii, M. B. Smirnov, K. S. Smirnov, R. Baddour-Hadjean, J.-P. Pereira-Ramos, A. N. Smirnov, V. Y. Davydov, A computational and spectroscopic study of the electronic structure of v2o5-based cathode materials, The Journal of Physical Chemistry C 125 (10) (2021) 5848–5858. doi:10.1021/acs.jpcc.0c11285.

[35] H. R. Chandrasekhar, G. Bhattacharya, R. Migoni, H. Bilz, Infrared and Raman spectra and lattice dynamics of the superionic conductor, Physical Review B 17 (2) (1978) 884–893. doi:10.1103/PhysRevB.17.884.
URL https://link.aps.org/doi/10.1103/PhysRevB.17.884

[36] S. I. U. Shah, A. L. Hector, X. Li, J. R. Owen, Solvothermal synthesis and electrochemical charge storage assessment of Mn3N2, Journal of Materials Chemistry A 3 (7) (2015) 3612–3619. doi:10.1039/c4ta05316h.

[37] Y. Takeuchi, T. Yamashita, K. Kuriyama, K. Kushida, Synthesis and charge-discharge performance of Li5SiN3 as a cathode material of lithium secondary batteries, Journal of Solid State Electrochemistry 20 (7) (2016) 1885–1888. doi:10.1007/s10008-016-3131-9.

[38] K. Kuriyama, Y. Suzuki, K. Kushida, Small polaron transport in Li_7MnN_4 containing isolated MnN_4 tetrahedra, Solid State Communications 148 (11-12) (2008) 508–510. doi:10.1016/j.ssc.2008.10.001.

[39] S. Suzuki, Electronic structure and electrochemical properties of electrode material $Li_{7-x}MnN_4$, Solid State Ionics 116 (1-2) (1999) 1–9. doi:10.1016/S0167-2738(98)00337-3.

[40] K. Wilayat, R. A.H., First principles treatment of structural, optical, and thermoelectric properties of Li_7MnN_4 as electrode for a Li secondary battery, Materials Research Bulletin 61 (2015) 306–314. doi:10.1016/j.materresbull.2014.10.021.

[41] K. Kushida, Y. Ichihashi, Y. Suzuki, K. Kuriyama, Electronic structural difference between Li_7VN_4 and Li_7MnN_4 due to the replacement of V with Mn: A simulation by a discrete variational Xα method, Physica B: Condensed Matter 405 (9) (2010) 2305–2310. doi:10.1016/j.physb.2010.02.033.

[42] A. C. Larson, R. B. V. Dreele, General structure analysis system (GSAS), Los Alamos National Laboratory, Technical Report No. LAUR86-748 (2004) 231.

[43] B. H. Toby, EXPGUI , a graphical user interface for GSAS, Journal of Applied Crystallography 34 (2) (2001) 210–213. doi:10.1107/S0021889801002242.

[44] E. Panabière, N. Emery, S. Bach, J.-P. Pereira-Ramos, P. Willmann, Investigation of the chemical stability of Li_7MnN_4 in air, Corrosion Science 77 (2013) 64–68. doi:10.1016/j.corsci.2013.07.027.

[45] R. Dovesi, A. Erba, R. Orlando, C. M. Zicovich-Wilson, B. Civalleri, L. Maschio, M. Rérat, S. Casassa, J. Baima, S. Salustro, B. Kirtman, Quantum-mechanical condensed matter simulations with CRYSTAL, WIREs Computational Molecular Science 8 (4) (2018) 1–36. doi:10.1002/wcms.1360.

[46] R. Dovesi, V. R. Saunders, C. Roetti, R. Orlando, C. M. Zicovich-Wilson, F. Pascale, B. Civalleri, K. Doll, N. M. Harrison, I. J. Bush, P. D'Arco, M. Llunell, M. Causá, Y. Noël, CRYSTAL17 User's Manual, University of Torino, Torino, 2017.

[47] D. V. Oliveira, J. Laun, M. F. Peintinger, T. Bredow, BSSE-correction scheme for consistent gaussian basis sets of double- and triple-zeta valence with polarization quality for solid-state calculations, Journal of Computational Chemistry 40 (27) (2019) 2364–2376. doi:10.1002/jcc.26013.

[48] J. P. Perdew, A. Ruzsinszky, G. I. Csonka, O. A. Vydrov, G. E. Scuseria, L. A. Constantin, X. Zhou, K. Burke, Restoring the density-gradient expansion for exchange in solids and surfaces, Physical Review Letters 100 (13) (2008) 136406. doi:10.1103/physrevlett.100.136406.
URL http://dx.doi.org/10.1103/PhysRevLett.100.136406

[49] H. J. Monkhorst, J. D. Pack, Special points for brillouin-zone integrations, Physical Review B 13 (12) (1976) 5188–5192. doi:10.1103/physrevb.13.5188.
URL http://dx.doi.org/10.1103/PhysRevB.13.5188

[50] F. Pascale, C. M. Zicovich-Wilson, F. L. Gejo, B. Civalleri, R. Orlando, R. Dovesi, The calculation of the vibrational frequencies of crystalline compounds and its implementation in the CRYSTAL code, Journal of Computational Chemistry 25 (6) (2004) 888–897. doi:10.1002/jcc.20019.

[51] M. Ferrero, M. Rérat, B. Kirtman, R. Dovesi, Calculation of first and second static hyperpolarizabilities of one- to three-dimensional periodic compounds. implementation in the CRYSTAL code., The Journal of Chemical Physics 129 (24) (2008) 244110. doi:10.1063/1.3043366.

[52] D. A. Long, The Raman effect: A unified treatment of the theory of Raman scattering by molecules, WILEY, 2002.
URL https://www.ebook.de/de/product/1377890/derek_a_long_the_raman_effect_a_unified_treatment_of_the_theory_of_raman_scattering_by_molecules.html

[53] A. Togo, I. Tanaka, First principles phonon calculations in materials science, Scripta Materialia 108 (2015) 1–5. doi:10.1016/j.scriptamat.2015.07.021.

[54] P. Borlido, T. Aull, A. W. Huran, F. Tran, M. A. L. Marques, S. Botti, Large-scale benchmark of exchangeâcorrelation functionals for the determination of electronic band gaps of solids, J. Chem. Theory Comput. 15 (9) (2019) 5069–5079. doi:10.1021/acs.jctc.9b00322.
URL https://doi.org/10.1021/acs.jctc.9b00322

[55] A. Liang, R. Turnbull, P. Rodríguez-Hernandez, A. Muñoz, M. Jasmin, L.-T. Shi, D. Errandonea, General relationship between the band-gap energy and iodine-oxygen bond distance in metal iodates, Physical Review Materials 6 (4) (apr 2022). doi:10.1103/physrevmaterials.6.044603.

[56] M. I. Aroyo, J. M. Perez-Mato, C. Capillas, E. Kroumova, S. Ivantchev, G. Madariaga, A. Kirov, H. Wondratschek, Bilbao Crystallographic Server: I. Databases and crystallographic computing programs, Zeitschrift für Kristallographie - Crystalline Materials 221 (1) (2006) 15–27. doi:10.1524/zkri.2006.221.1.15.

[57] R. D. Shannon, Revised effective ionic radii and systematic studies of interatomic distances in halides and chalcogenides, Acta Cryst. A32 (5) (1976) 751–767. doi:10.1107/S0567739476001551.
URL https://doi.org/10.1107/S0567739476001551

[58] A. A. B. Baloch, S. M. Alqahtani, F. Mumtaz, A. H. Muqaibel, S. N. Rashkeev, F. H. Alharbi, Extending shannon's ionic radii database using machine learning, Phys. Rev. Materials 5 (2021) 043804. doi:10.1103/PhysRevMaterials.5.043804.
URL https://link.aps.org/doi/10.1103/PhysRevMaterials.5.043804

[59] A. Bhatia, Y. Dridi Zrelli, J. P. Pereira-Ramos, R. Baddour-Hadjean, Detailed redox mechanism and self-discharge diagnostic of 4.9 V LiMn1.5Ni0.5O4spinel cathode revealed by Raman spectroscopy, Journal of Materials Chemistry A 9 (23) (2021) 13496–13505. doi:10.1039/d1ta00989c.